



Article

Heterojunction Devices Fabricated from Sprayed *n*-Type Ga₂O₃, Combined with Sputtered *p*-Type NiO and Cu₂O

Theodoros Dimopoulos ^{1,*} , Rachmat Adhi Wibowo ¹ , Stefan Edinger ¹ , Maximilian Wolf ¹ and Thomas Fix ²

¹ Energy Conversion and Hydrogen Technologies, Center for Energy, AIT Austrian Institute of Technology, Giefinggasse 2, 1210 Vienna, Austria; rachmat.wibowo@ait.ac.at (R.A.W.); stefan.edinger@ait.ac.at (S.E.); maximilian.wolf@ait.ac.at (M.W.)

² ICube Laboratory, Université de Strasbourg and Centre National de la Recherche Scientifique (CNRS), 23 Rue Du Loess, BP 20 CR, F-67037 Cedex 2 Strasbourg, France; tfix@unistra.fr

* Correspondence: theodoros.dimopoulos@ait.ac.at

Abstract: This work reports on the properties of heterojunctions consisting of *n*-type Ga₂O₃ layers, deposited using ultrasonic spray pyrolysis at high temperature from water-based solution, combined with *p*-type NiO and Cu₂O counterparts, deposited by radio frequency and reactive, direct-current magnetron sputtering, respectively. After a comprehensive investigation of the properties of the single layers, the fabricated junctions on indium tin oxide (ITO)-coated glass showed high rectification, with an open circuit voltage of 940 mV for Ga₂O₃/Cu₂O and 220 mV for Ga₂O₃/NiO under simulated solar illumination. This demonstrates in praxis the favorable band alignment between the sprayed Ga₂O₃ and Cu₂O, with small conduction band offset, and the large offsets anticipated for both energy bands in the case of Ga₂O₃/NiO. Large differences in the ideality factors between the two types of heterojunctions were observed, suggestive of distinctive properties of the heterointerface. Further, it is shown that the interface between the high-temperature-deposited Ga₂O₃ and the ITO contact does not impede electron transport, opening new possibilities for the design of solar cell and optoelectronic device architectures.

Keywords: cuprous oxide; gallium oxide; nickel oxide; heterojunctions; sputtering; spray pyrolysis; electron transport layers; hole transport layers; solar cells



Citation: Dimopoulos, T.; Wibowo, R.A.; Edinger, S.; Wolf, M.; Fix, T. Heterojunction Devices Fabricated from Sprayed *n*-Type Ga₂O₃, Combined with Sputtered *p*-Type NiO and Cu₂O. *Nanomaterials* **2024**, *14*, 300. <https://doi.org/10.3390/nano14030300>

Academic Editor: Zhan'ao Tan

Received: 16 December 2023

Revised: 26 January 2024

Accepted: 27 January 2024

Published: 1 February 2024



Copyright: © 2024 by the authors. Licensee MDPI, Basel, Switzerland. This article is an open access article distributed under the terms and conditions of the Creative Commons Attribution (CC BY) license (<https://creativecommons.org/licenses/by/4.0/>).

1. Introduction

By virtue of their versatile, wide-ranging electronic properties, metal oxide semiconductors are indispensable materials for a wide range of devices, including photovoltaic (PV) and photoelectrochemical cells, organic light-emitting diodes (OLEDs) and photodetectors, or power electronics components. They provide functionalities as transparent electrodes, charge-carrier-selective transport or injection layers, as well as light absorbers, depending on their electrical conductivity, work function, and bandgap. Nickel oxide (NiO), a *p*-type wide bandgap (3.4–3.7 eV) semiconductor, bears a high potential to replace organic hole transport layers in perovskite and organic photovoltaic devices, as elaborated in many recent reviews [1–5]. Cuprous oxide (Cu₂O), also a *p*-type material, with a bandgap of 1.9–2.6 eV, has been introduced as a hole-transport layer in perovskite cells [6], recently achieving very promising efficiency and stability results [7]. Because of its relatively low bandgap, it has been widely investigated as a light absorber in all-oxide solar cells [8], as well as in photoelectrochemical cells for water splitting [9]. Gallium oxide (Ga₂O₃), on the other hand, is an *n*-type, wide-bandgap (4.8–5.0 eV) semiconductor that has demonstrated high potential in solar cells when combined with Cu₂O, as will be elaborated later. However, it has also found implementation as an electron-transport layer in perovskite solar cells [10]. Heterojunctions between Ga₂O₃ and NiO or Cu₂O are of interest, both from a fundamental and applications points of view.

$\text{Ga}_2\text{O}_3/\text{NiO}$ junctions have been investigated in the literature, mainly for applications in power electronics, as summarized in a recent review [11]. In these devices, NiO thin films have been deposited on single-crystal Ga_2O_3 substrates or thick (several micrometers) Ga_2O_3 layers [12–15], with different techniques, including sol-gel [12], atomic layer deposition (ALD) [13], and radio-frequency (RF) sputtering [13,14]. The reverse architecture has also been reported: Wang et al. [16] sputter-deposited 4 μm thick films of NiO, combined with sputtered 200 nm thick Ga_2O_3 films, for use as self-powered photodetectors. In all of these works, a type II band alignment at the heterojunction has been shown, with conduction band offset (CBO) between 0.9 and 2.7 eV and valence band offset (VBO) between 2.1 and 3.6 eV [12–17]. This wide spread of values shows the sensitivity of the energy band alignment on the material's processing, crystal orientation, and other factors. However, such thick films cannot be applied as electron and hole transport layers in PV or OLED devices and reducing the thickness to the tens of nanometers regime—or further—is challenging for the structural integrity of the layers and, therefore, the operation of the device.

The interest in $\text{Cu}_2\text{O}/\text{Ga}_2\text{O}_3$ heterojunctions has increased in the last decade, since Minami et al. reported high-efficiency (~5.4%) $\text{Cu}_2\text{O}/\text{Ga}_2\text{O}_3$ solar cells, using thermal oxidation of Cu sheets at high temperatures for the preparation of Cu_2O and pulsed laser deposition for Ga_2O_3 . The high efficiency is caused by the optimum conduction band alignment between the *p* and *n* layers [18]. A bit later, Lee et al. reported 1.2 V open circuit voltage and efficiency of ~4% in $\text{Cu}_2\text{O}/\text{Ga}_2\text{O}_3$ heterojunctions with electrodeposited Cu_2O and Ga_2O_3 fabricated by ALD, with optimized band alignment and passivation of interface defects [19]. Chua et al. showed that, when growing Ga_2O_3 by ALD on top of Cu_2O grown by chemical vapor deposition (CVD), exposure to air is of vital importance for the transport properties, as a CuO layer forms on the Cu_2O . By avoiding air exposure between the deposition of the two layers, they could enhance the open circuit voltage from 1.4 V to ~1.8 V [20]. From these works, one can conclude that, from the point of view of interface stoichiometry control, it is advantageous to deposit Cu_2O on Ga_2O_3 and not vice versa, unless the surface oxidation of Cu_2O can be avoided. Benz et al. fabricated both oxide layers by sputtering and investigated the VBO and CBO at the interface. They found that $\alpha\text{-Ga}_2\text{O}_3/\text{Cu}_2\text{O}$ has the lowest CBO of ~0.2 eV and a VBO of ~3.2 eV, while, in $\beta\text{-Ga}_2\text{O}_3/\text{Cu}_2\text{O}$ junctions, the CBO increases to ~1.3 eV and the VBO to ~3.7 eV. To this respect, they claimed that the use of $\alpha\text{-Ga}_2\text{O}_3$ bears the highest potential for application in solar cells in combination with Cu_2O [21]. Their work, however, did not show electrical characterization of the junctions.

The present work reports for the first time the properties of heterojunctions composed of *n*-type Ga_2O_3 layers deposited by ultrasonic spray pyrolysis [22], in combination with RF- and DC-sputtered *p*-type NiO and Cu_2O counterparts, respectively. The structural, optical, and electronic properties of the single layers are investigated before the analysis of the electrical transport characteristics of the junctions in the dark and under simulated solar light, yielding information about the energy band alignment in the two junction types.

2. Materials and Methods

Three types of substrates were used in this study: the first was uncoated borosilicate glass (NEXTERION[®] D, 1.0 mm thickness, cut in 25 × 25 mm size, Schott, Jena, Germany), used for the deposition of Ga_2O_3 by spray-pyrolysis, due to its superior thermal stability. The second was uncoated, soda-lime, microscope slides (size: 25 × 25 × 1.0 mm, Menzel Gläser, Braunschweig, Germany), used for the deposition of the sputtered layers, and the third was ITO-coated glass (size: 25 × 25 × 1.1 mm, Product No. 703192, Merck, Darmstadt, Germany) with a sheet resistance of 8–12 Ω/sq , used for the deposition of devices.

For the patterning of the ITO-coated substrates, the following procedure was followed: polyimide film tape (Kapton[®], DuPont Teijin Films, Chester, VA, USA) with a width of 12.5 mm was used to cover a middle stripe of the ITO, before immersing the substrate into a 9 M HCl aqueous solution (1:1 dilution), etching away the ITO from the uncovered area.

After the etching, the substrate was rinsed with ultrapure water (resistivity: 18 M Ω -cm, Arium[®], Göttingen, Germany) and the tape was removed. The substrate was then thoroughly cleaned by ultrasonication in a bath with ultrapure water and cleaning concentrate (HelmanexTM III, Merck, Darmstadt, Germany), under sonication at 50 °C, followed by sonication in ultrapure water and, finally in isopropanol (each step for a 15 min duration), before being blown-dry in nitrogen stream. The same cleaning procedure was applied for the bare glass substrates.

The substrates were then transferred to the spray pyrolysis setup (Sono-Tek ExactaCoat[®], equipped with a Sono-Tek Impact[®] ultrasonic nozzle operating at 120 kHz, Sono-Tek Corporation, Milton, NY, USA), where they were heated to 380 °C and coated with Ga₂O₃, following the process described in [22]. The layer thickness range was between 12 and 30 nm. For the Ga₂O₃ deposition on the ITO substrate, a layer thickness of 15 nm was chosen. A 3 mm wide stripe was left uncoated on one side of the ITO substrate to be later used as back-side contact. After the Ga₂O₃ deposition, the substrates were left to cool down to ~50 °C, before being taken off the hotplate. After the spray-pyrolysis, due to the applied thermal budget, the ITO substrate's sheet resistance increased to $51 \pm 6 \Omega/\text{sq}$.

For the sputtering, a Leybold Univex cluster tool was used (Leybold, Cologne, Germany). All layers were deposited without substrate heating at a substrate-to-target distance of ~9 cm. The deposition of NiO was carried out using a NiO target (101.6 mm diameter, 99.99% purity, AJA Int., Scituate, MA, USA), mounted on an RF magnetron source. The applied sputter power was 200 W and pure Ar was used as process gas at a pressure of 10 μ bar, resulting in a sputter rate of 0.11 nm/s. Layers of 20–40 nm in thickness were deposited. The deposition of Cu₂O was carried out using a metallic Cu target (101.6 mm diameter, 99.995% purity, Materion, Mayfield Heights, OH, USA), mounted on a DC magnetron source. A sputter power of 80 W was applied for the deposition in an atmosphere of Ar/O₂:80/20 at a pressure of 10 μ bar. Prior to each deposition process, the target was sputtered in pure Ar atmosphere at 120 W and 5 μ bar pressure for at least 10 min, followed by 5 min in Ar/O₂ atmosphere at 80 W. This step served to condition and clean the target from the oxide and achieve reproducible deposition results with pure Cu₂O phase. At these conditions, the sputter rate was 0.74 nm/s. The deposition of the device contacts was carried out using an Au target (76 mm diameter, 99.99% purity, Neyco, Vanves, France) at 20 W and 2 μ bar Ar pressure, resulting in a rate of 0.8 nm/s. The contacts were sputtered through a shadow mask, defining active device areas of 5.73 mm² and 10.43 mm².

The sputter deposition rates for NiO and Cu₂O were extracted by measuring the layer thickness (step height) using a surface profilometer (Alpha-Step[®] IQ, KLA-Tencor, Milpitas, CA, USA). The morphology of the layers was measured by scanning electron microscopy (SEM) (Zeiss Ultra 40, Zeiss, Oberkochen, Germany) with a beam accelerating voltage of 5 kV and an in-lens detector. The surface topography was evaluated by atomic force microscopy (AFM) (PicoPlus, Molecular Imaging, Tempe, AZ, USA) in tapping mode, using SSS-NCHR probes (NanosensorsTM, Neuchatel, Switzerland). The open-source software Gwyddion, version 2.61, was used to plot and analyze the AFM data. Structural characterization of the layers was realized using a grazing incidence X-ray diffractometer (XRD) (ARL Equinox 100, Thermo Fisher Scientific, Waltham, MA, USA) at an angle of 5 °, with Cu-K α radiation. The analysis of the diffractograms was conducted using the Match! Software, version 3.14 (Crystal Impact, Bonn, Germany), with reference databases from Crystallographic Open Database (COD).

Transmission and reflectance spectra were recorded by a Fourier transform spectrometer (FTS) (Bruker, Billerica, MA, USA, Vertex 70) equipped with a halogen lamp as a source of unpolarized light (64642 HLX, Osram Licht, Munich, Germany). Direct transmittance was measured at normal incidence in reference to air and reflectance was measured at an incidence angle of 13° in reference to a calibrated mirror (STAN-SSH-NIST, Ocean Optics, Orlando, FL, USA). A GaP and a Si diode detector were used for the spectral ranges of 303–588 nm and 500–1205 nm, respectively.

Optical simulations were performed using a transfer matrix method (TMM) algorithm, described by Ebner et al. [23]. The sheet resistance was determined using an in-line four-point probe (Nagy SD-600, Nagy Instruments, Gäufelden, Germany). Current density–voltage (j - V) curves of solar cells were obtained with two-point measurements, using a semiconductor parameter analyzer (4156C, Agilent Technologies, Santa Clara, CA, USA) under dark and AM1.5G-simulated illumination (LOT-Oriel solar simulator, Darmstadt, Germany). For the capacitance–voltage (C - V) measurements, an LCR Meter was used (4284A, Agilent Technologies, Santa Clara, CA, USA).

For the determination of the work function (WF) and ionization energy (IE) of the layers, Kelvin probe and ambient pressure photoemission spectroscopy (APS) were performed in air (KP Technology, Wick, UK, APS03). A 2 mm diameter Au-coated tip was calibrated using air photoemission. The WF of the material was determined by measuring the contact potential difference between the Kelvin probe tip and the surface of the sample. The IE was measured using the same system by photoelectron emission. Finally, for the electrochemical impedance spectroscopy (EIS), a 3-electrode cell was used, with the coated sample serving as a working electrode, platinized Ti mesh as a counter electrode, and Ag/AgCl as reference. The cell was connected to a potentiostat (Vionic, Metrohm, Herisau, Switzerland). A 0.5 M Na_2SO_4 aqueous electrolyte was used.

3. Results

3.1. AFM and SEM Characterization

AFM characterization was realized for layers deposited on glass substrates. All layers have low roughness, with fine grain structure, making them suitable for implementation in ultra-thin solar cells and optoelectronic devices. The largest roughness is measured for Ga_2O_3 : the 30 nm thick layer yields RMS roughness of 2.0 nm (Figure 1a), with the background roughness of the borosilicate glass being 0.3 nm (Figure S1a). The lowest roughness is measured for NiO: the 40 nm thick layer yields RMS roughness of 0.9 nm (Figure 1b), the same as the background roughness of the glass substrate (Figure S1b). The RMS value for the 40 nm thick Cu_2O is 1.6 nm (Figure 1c), with a grain size considerably larger than for Ga_2O_3 and NiO.

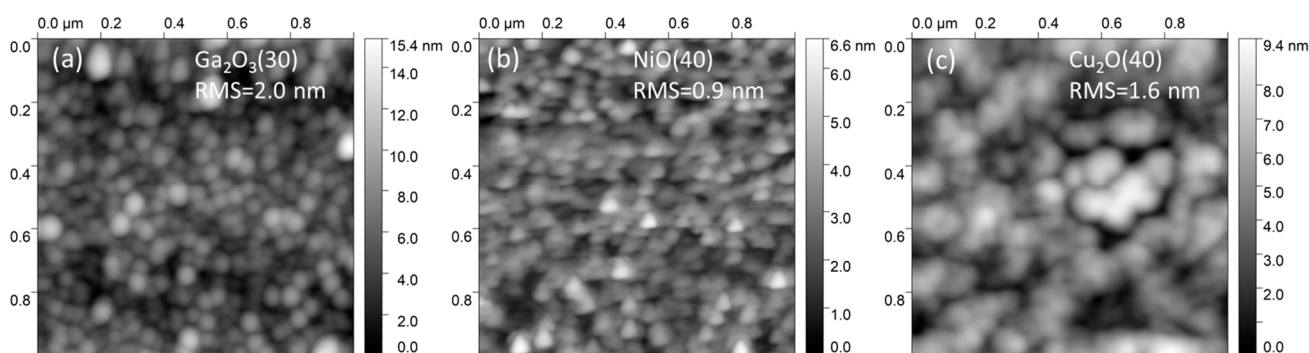


Figure 1. AFM images of single layers of: (a) $\text{Ga}_2\text{O}_3(30)$, (b) $\text{NiO}(40)$, and (c) $\text{Cu}_2\text{O}(40)$, along with the corresponding RMS roughness values.

The heterojunction multilayers also feature low roughness. Figure 2 shows the roughness evolution with the sequential deposition of layers. The ITO back electrode (heated to the temperature used for the Ga_2O_3 deposition, i.e., 380 °C) has an RMS value of 2.2 nm. The deposition of 15 nm Ga_2O_3 atop, leads to a marginal increase in the RMS to 2.4 nm. The RMS further increases moderately with the deposition of the 20 nm NiO, reaching 2.8 nm. On the other hand, 100 nm of Cu_2O brings the RMS to 2.6 nm, increasing to 4.1 nm when a 300 nm Cu_2O film is deposited. The AFM images suggest that, with the increase in Cu_2O thickness, the film acquires a more compact character, which helps to keep the overall roughness of the stack at low levels.

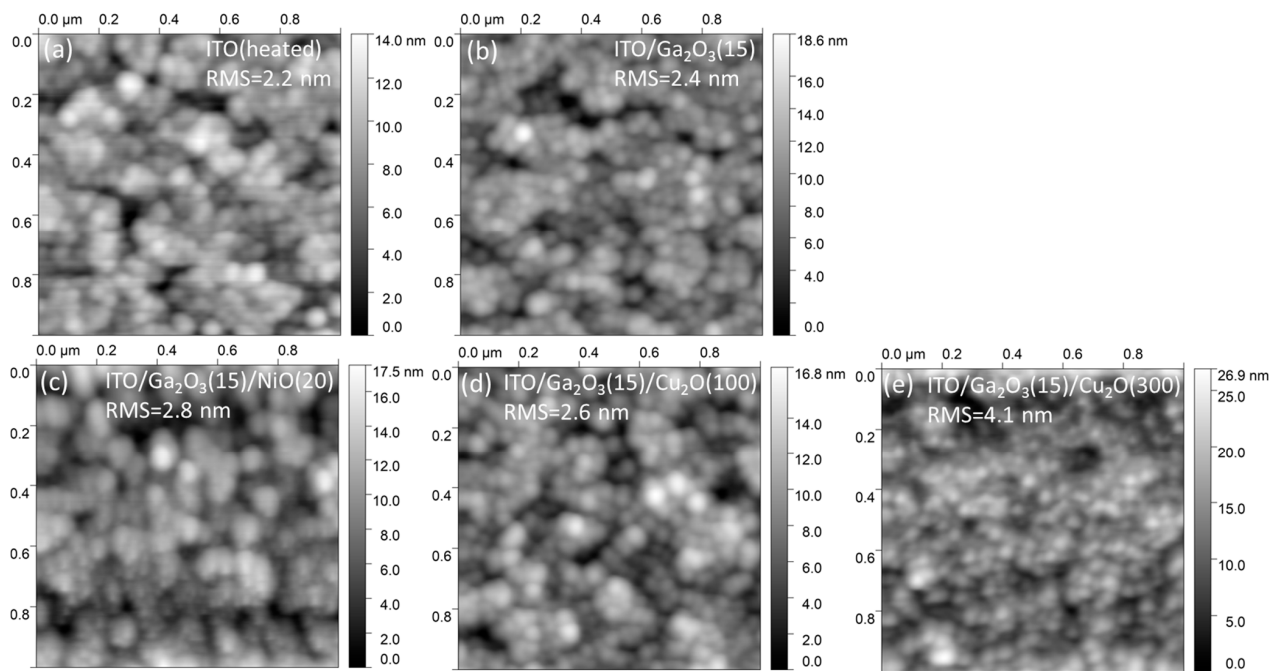


Figure 2. AFM images of the: (a) ITO substrate, (b) ITO/Ga₂O₃(15), (c) ITO/Ga₂O₃(15)/NiO(20), (d) ITO/Ga₂O₃(15)/Cu₂O(100), and (e) ITO/Ga₂O₃(15)/Cu₂O(300) stacks, along with the obtained RMS roughness values.

The compact character of the layers can be further evidenced in the cross-section SEM images, shown in Figure 3. One can clearly distinguish the ITO layer with a thickness of ~125 nm, followed by the compact and continuous Ga₂O₃ interfacial layer and the NiO, having a combined thickness of ~35 nm (Figure 3a). On the other hand, for the sample in Figure 3b, the Cu₂O layer has a thickness of ~300 nm. The plain-view SEM images (Figure 3c,d) show again very different grain structures between the ultra-thin NiO and the thick Cu₂O.

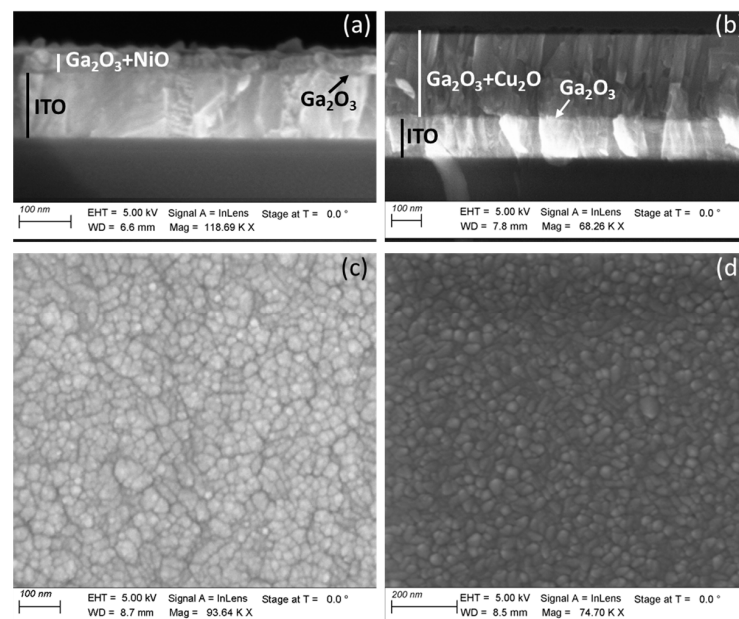


Figure 3. Cross-section and plain-view SEM images of the (a), (c) ITO/Ga₂O₃(15)/NiO(20) and (b), (d) ITO/Ga₂O₃(15)/Cu₂O(300) stacks.

3.2. Structural Characterization

Single NiO and Cu₂O layers of different thicknesses were deposited on plain glass substrates for XRD characterization. As described in [22], relatively thick (>150 nm) spray-pyrolyzed Ga₂O₃ layers adopt the monoclinic β -Ga₂O₃ structure, with predominant (111) texturing. However, GIXRD diffractograms of thin films of the order used in this work (15–30 nm) show no reflection peaks (apart from the broad background of the glass substrate on which they were deposited).

For the NiO layers, down to a thickness of 20 nm, crystalline structure reflections can be observed (Figure 4a). For the 100 nm film, the pattern is composed of the (111), (200), (202), and (311) peaks, with the (200) and (111) being the most prominent, in agreement with the reference for cubic NiO (Fm $\bar{3}$ m, COD: 96-432-0506). For the 40 nm film, the (200), (111), and (202) peaks are clearly visible and, even for the 20 nm thick film, the (200) peak can still be distinguished. The structure of the RF-sputtered films agree with various reports from the literature implementing DC or RF mode sputtering in Ar and Ar/O₂ atmosphere [24–26].

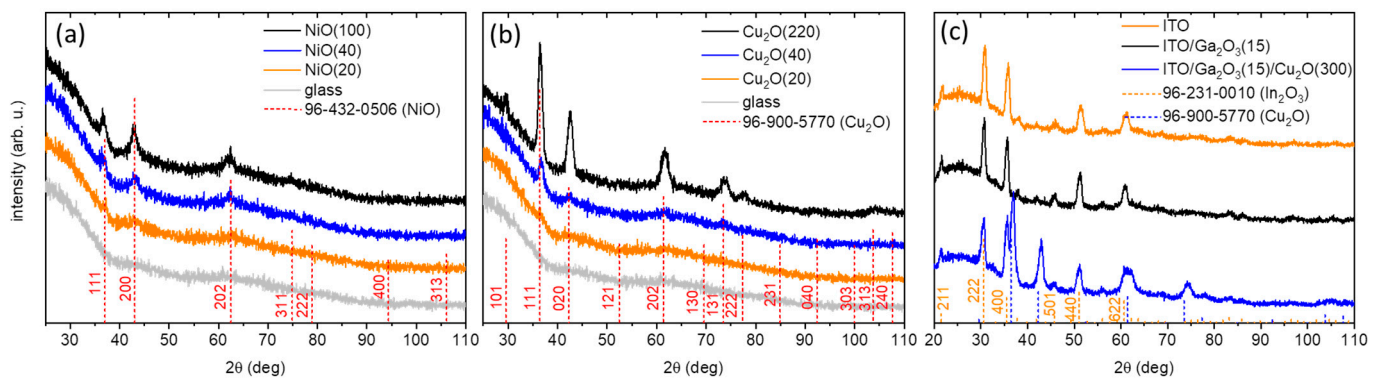


Figure 4. GIXRD patterns of the (a) NiO and (b) Cu₂O single films of different thicknesses. (c) GIXRD patterns of the ITO, ITO/Ga₂O₃(15), and ITO/Ga₂O₃(15)/Cu₂O(300) stacks.

The Cu₂O 220 nm thick film yields a pattern that perfectly matches the cuprite cubic reference (Pn $\bar{3}$ m, COD: 96-900-5770), with high-intensity (111), (020), and (202) peaks, underlining the polycrystalline character of the deposit (Figure 4b). Similar results were obtained by reactive DC sputtering of Cu₂O from a Cu target in the literature [27]. A clear pattern is also distinguished for the 40 nm film, with the aforementioned reflections present. For the 20 nm film, no reflections are visible. In conclusion, the GIXRD characterization demonstrates the crystalline nature of the NiO and Cu₂O, as well as the phase purity, as no foreign reflections were detected.

Figure 4c shows the GIXRD pattern of the ITO substrate, corresponding to the cubic structure (Ia $\bar{3}$, COD: 96-231-0010). After the deposition of the Ga₂O₃ layer at high temperature, the reflection peaks of the ITO remain unchanged and no additional peaks can be observed. For the complete ITO/Ga₂O₃/Cu₂O(300) multilayer, both In₂O₃ and Cu₂O patterns can be clearly distinguished. The same polycrystalline pattern is obtained for the Cu₂O on the ITO/Ga₂O₃ substrate as on the glass, which is not always the case for sputtered Cu₂O films [28]. It is noted, however, that, in this case, the Cu₂O peaks are all slightly shifted to the right with respect to the reference and the single films, which can be attributed to an induced stress when the layer is deposited on top of the ITO/Ga₂O₃ substrate.

3.3. Optical Characterization

To extract the refractive index from optical spectra, single layers of the oxides with a thickness below 50 nm were deposited to avoid light interference patterns in the spectra that can complicate the index determination procedure. Figure 5a–c show transmittance (*T*), reflectance (*R*), and absorbance ($A = 1 - T - R$) spectra for the Ga₂O₃(30), NiO(40), and Cu₂O (40) layers, respectively (for Ga₂O₃, *A* is practically zero). All spectra are referenced

to air. Each graph also includes the T and R spectra of the glass substrates. The Ga_2O_3 layer is highly transparent over the whole spectrum, while NiO presents considerable absorption losses for wavelengths < 600 nm. In the same spectral region, as expected, Cu_2O presents strong absorption. Considering the refractive index of the glass $n_G = 1.52$ and air as the surrounding medium ($n_{\text{air}} = 1.00$), the transfer matrix method (TMM) was used to calculate the complex refractive index of the materials in the range 400–1000 nm, as shown in Figure 5d–f. Due to the negligible absorption, only the real part of the refractive index is plotted for Ga_2O_3 , with n decreasing continuously with the wavelength from 1.89 at 400 nm to 1.72 at 1000 nm. The results are in line with the literature reports for Ga_2O_3 layers fabricated by different techniques like sputtering [29] or plasma-enhanced atomic layer deposition [30].

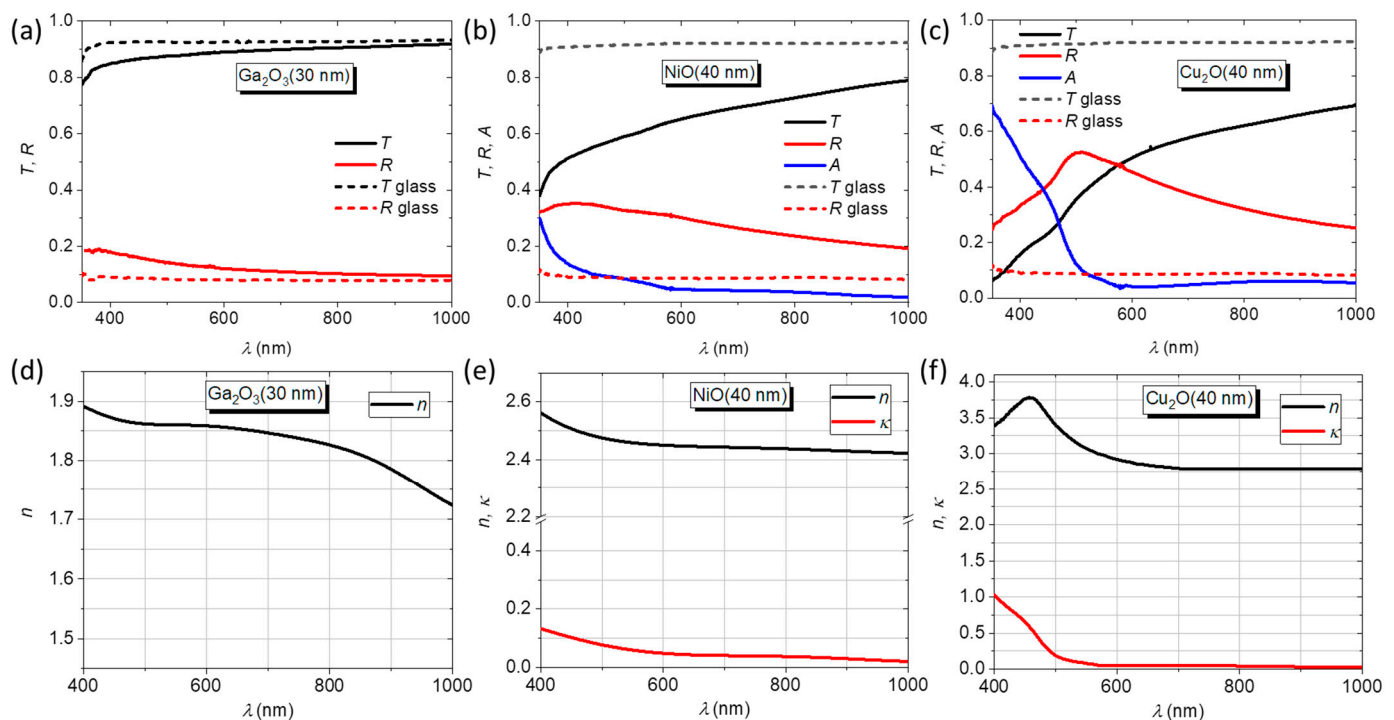


Figure 5. Transmittance (T), reflectance (R), and absorbance (A) spectra for single layers of (a) $\text{Ga}_2\text{O}_3(30)$, (b) $\text{NiO}(40)$, and (c) $\text{Cu}_2\text{O}(40)$, together with the T and R of the respective glass substrates. The second row shows the calculated refractive index and extinction coefficient for (d) Ga_2O_3 , (e) NiO , and (f) Cu_2O .

A significantly larger n is calculated for NiO , decreasing from 2.57 at 400 nm to 2.42 at 1000 nm. The extinction coefficient κ decreases with the wavelength from $\kappa = 0.14$ at 400 nm to 0.017. Likewise, the refractive index of the NiO layer agrees with literature results from spectroscopic ellipsometry measurements of reactively sputtered NiO films [31]. For Cu_2O , n maximizes to the value of 3.79 at 450 nm and reaches a plateau at 2.79 above 700 nm. The extinction coefficient has the value of 1.00 at 400 nm, dropping to 0.055 for $\lambda > 600$ nm. The extracted complex refractive index of Cu_2O agrees very well with reported values for bulk material measured by spectroscopic ellipsometry [32], indicating the high optical quality of the sputtered films.

The bandgap of the sprayed Ga_2O_3 was previously reported to be ~ 5.0 eV [22]. Here, the bandgap values of NiO and Cu_2O are calculated from the optical spectra of thicker films (Figure 6a,b), using the Tauc plot method [33]. For this, the absorption coefficient is obtained from the relation [34]:

$$\alpha = \frac{1}{t} \ln \left(\frac{1-R}{T} \right),$$

where t is the film thickness. The relation $(\alpha h\nu)^m = C(h\nu - E_g)$ is used to fit the linear part of the plot $(\alpha h\nu)^m$ vs. $h\nu$, corresponding to the band-edge of the material. The factor m assumes the value of 2 for direct bandgap, 1/2 for indirect bandgap, and 2/3 for direct forbidden transition.

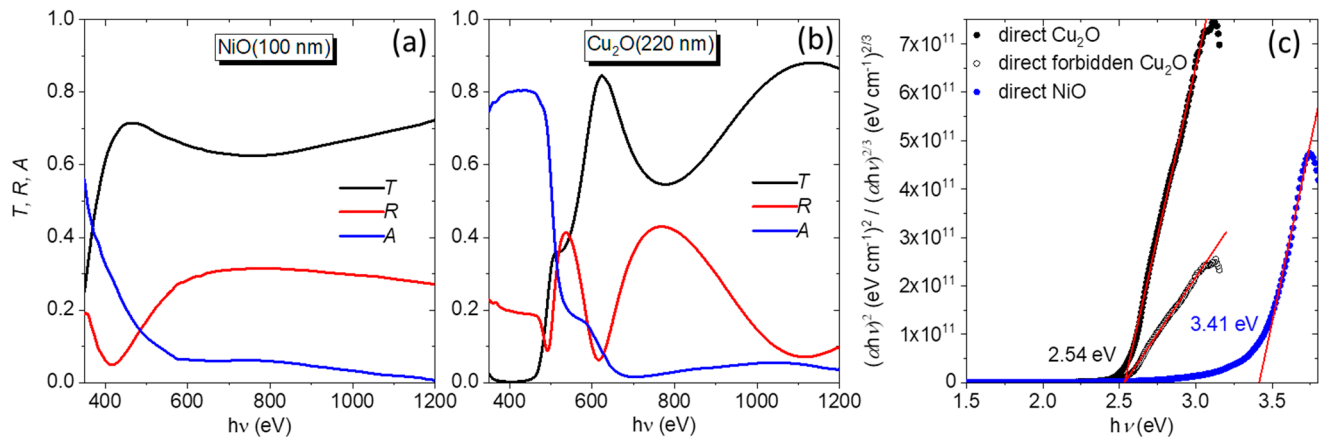


Figure 6. Transmittance, reflectance, and absorbance ($A = 1 - T - R$) spectra for (a) NiO(100) and (b) Cu₂O(220) layers. (c) Tauc plots for the bandgap estimation of the NiO and Cu₂O layers, assuming direct and direct forbidden transition for Cu₂O and direct transition for NiO. Also shown are the linear fits in the band-edge regions (red lines).

For NiO (Figure 6c), the best linear fit of the band edge is obtained for $m = 2$ (direct bandgap), giving rise to a bandgap value of 3.41 eV. This value is at the low end of the reported literature range for sputtered NiO films, which is 3.34–3.71 [24,35–37]. For Cu₂O (Figure 6c), an equally satisfactory linear fit in the band-edge region can be obtained if a direct allowed ($m = 2$) or direct forbidden ($m = 2/3$) transition is considered, with the latter being a more realistic assumption for this material [38]. In both cases, the bandgap value is $E_g = 2.54$ eV, as can be seen in Figure 6c. This value is in the upper end of the range reported for Cu₂O layers, prepared by sputtering, which is between 2.18 and 2.58 eV [39–41]. A general conclusion in the literature is that the widening of the Cu₂O bandgap relates to the reduction in defects and enhanced crystallization, which were achieved with the help of annealing [40,41] or the use of mixed O₂-N₂ reactive gas during deposition [39].

Figure 7 shows optical spectra for the heterojunctions at sequential stages of their deposition. Interestingly, the transmittance of the glass/ITO substrate that is coated with the Ga₂O₃(15) layer is higher than the transmittance of the uncoated ITO (subjected to the thermal stress of the spray deposition). This is due to a reduction in the reflectance losses, as seen from the comparison of the two reflectance spectra in Figure 7. The deposition of the NiO(20) on the Ga₂O₃ reduces considerably the transmittance for $\lambda < 620$ nm due to the absorption of the NiO layer. The transmittance after the deposition of 100 nm Cu₂O shows enhanced absorption for $\lambda < 470$ nm and a subsequent gradual increase in the T as the band edge of the material is approached.

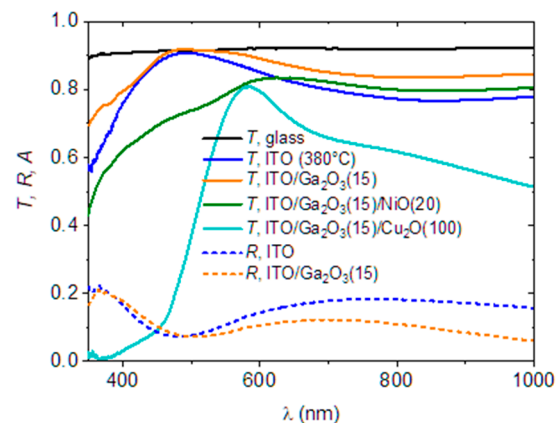


Figure 7. Transmittance, reflectance, and absorbance spectra for the heterojunctions at sequential stages of their deposition.

3.4. Electronic Properties Characterization

The Kelvin probe measurements yielded work function (WF) values of 4.8, 4.9, and 4.2 eV for Cu_2O , NiO , and Ga_2O_3 , respectively. The WF for Ga_2O_3 is 0.7 eV higher than the one previously extracted from UPS measurements [22]. It is known, however, that the two techniques give rise to distinctive values, as UPS measurements take place in ultra-high vacuum and Kelvin probe in air. Furthermore, the former gives a minimum value of the WF (as it is estimated by comparing the Fermi energy and the low-energy cut-off of the secondary electrons), while the latter gives an average over the probed electrode area. In addition, as pointed out in the introduction, the air-exposed surface of Cu_2O is covered with an atomically thin layer of CuO , which has a smaller WF than Cu_2O [42]. For this reason, the extracted value is only representative of the air-exposed Cu_2O but not of the surface formed upon Cu_2O deposition on Ga_2O_3 under vacuum. The ionization energy (IE) values, extracted from APS measurements, are 5.2 eV for both Cu_2O and NiO samples. For the Ga_2O_3 , the IE cannot be extracted from the APS, as it is below the measurable limit.

From the EIS measurements, at a frequency of $f = 1$ kHz, Mott–Schottky plots were constructed (Figure 8), showing negative slopes and, therefore, p -type conductivity for both Cu_2O and NiO layers. The hole carrier density N was extracted from the formula:

$$N = \frac{2}{qA^2\varepsilon_0\varepsilon \cdot S'}$$

where q is the electron charge, A the electrode area in the electrolyte, ε_0 the vacuum permittivity, ε the permittivity of the semiconductor (7.6 for Cu_2O and 11.9 for NiO) [43], and S the slope of the linear fit of the Mott–Schottky plot. Carrier density values of $5.2 \times 10^{24} \text{ m}^{-3}$ and $8.0 \times 10^{24} \text{ m}^{-3}$ for Cu_2O and NiO , respectively, were extracted, as shown in Figure 8a,b, respectively. These high carrier density values are in agreement with other works in the literature on sputtered Cu_2O [44] and NiO [31] films.

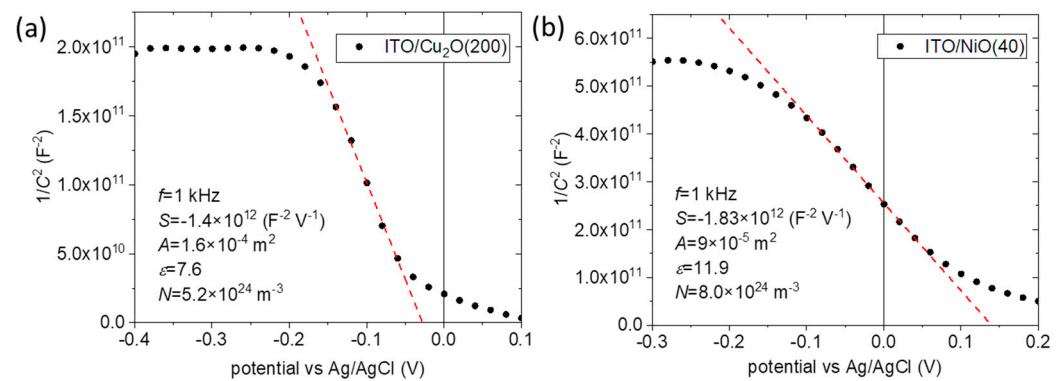


Figure 8. Mott–Schottky plots for the (a) ITO/Cu₂O(200) and (b) ITO/NiO(40) samples. The red lines are linear fits.

3.5. Heterojunction Characterization

For the heterojunctions, a standard Ga₂O₃ thickness of 15 nm was selected, based on an initial screening of the thickness-dependent performance, described in the Supplementary Information (Figure S2).

The properties of the ITO/Ga₂O₃(15)/NiO(20)/Au(100) heterojunctions were analyzed under dark and illuminated conditions. For a typical device, dark and illuminated j - V curves are shown in Figure 9a in a semilogarithmic scale (inset shows photo of a sample). The dark j - V shows large rectification (>1000 at $|V| = 0.5$ V), which demonstrates the formation of a high-quality n/p junction between the ultra-thin Ga₂O₃ and NiO layers. The dark j - V shows a low turn-on bias of ~ 30 mV in the forward direction (positive bias applied on the Au contact). The ideality factor n of the junction can be extracted from the fitting of the j - V curve for intermediate forward bias, in the range 0.16–0.36 V, using the diode equation:

$$j = j_0 \cdot \exp\left[\frac{qV}{nkT}\right],$$

which is derived as an approximation for the intermediate bias region of the general equation:

$$j = j_0 \cdot \left\{ \exp\left[\frac{q(V - j \cdot R_S^*)}{nkT}\right] - 1 \right\} + \frac{V - j \cdot R_S^*}{R_P^*},$$

where j_0 is the saturation current density, $R_S^* = R_S \cdot A$ and $R_P^* = R_P \cdot A$, with R_S and R_P being the series and the parallel resistance, respectively, and A the junction area, k the Boltzmann constant, and T the temperature. The first term in the above equation corresponds to the exponential diode current, whereas the second term is the shunt current, which can be approximated as V/R_P^* for reverse and low forward bias. The average ideality factor and standard deviation over five devices is $n = 1.6 \pm 0.2$. The ideality factor is, therefore, as expected from the Sah–Noyce–Shockley theory [45], in the regime between 1 and 2. The Ga₂O₃/NiO junction is a wide-gap, type II heterojunction with a large CB offset and an even larger VB offset. These large offsets block currents, so interface recombination is regarded as the dominant carrier transport channel across the heterojunction. The temperature dependence of the dark j - V characteristics was measured at 25, 40, 50, 60, 70, and 80 °C and the results are shown in Figure 9b. From the fitting in the intermediate forward voltage range, it is obtained that the ideality factor only slightly decreases with increasing temperature, as expected for the generation-recombination type of carrier transport. For the device shown in Figure 9, n decreases from 1.4 at ambient temperature to 1.3 at 80 °C (Figure 9b,f). From the fitting of the dark j - V curves in the region (−0.2, 0.1) V, a high parallel resistance is extracted, with a value of 11.7 MΩ cm² (Figure 9b). For all measured NiO solar cells, the parallel resistance was in the MΩ cm² range at ambient temperature. The illuminated curves show a very low short-circuit current

density of $j_{sc} = (3.0 \pm 0.5) \mu\text{A}/\text{cm}^2$, as expected from the minimal absorption of the high bandgap n and p counterparts. The open circuit voltage, V_{oc} , is $(224 \pm 11) \text{mV}$.

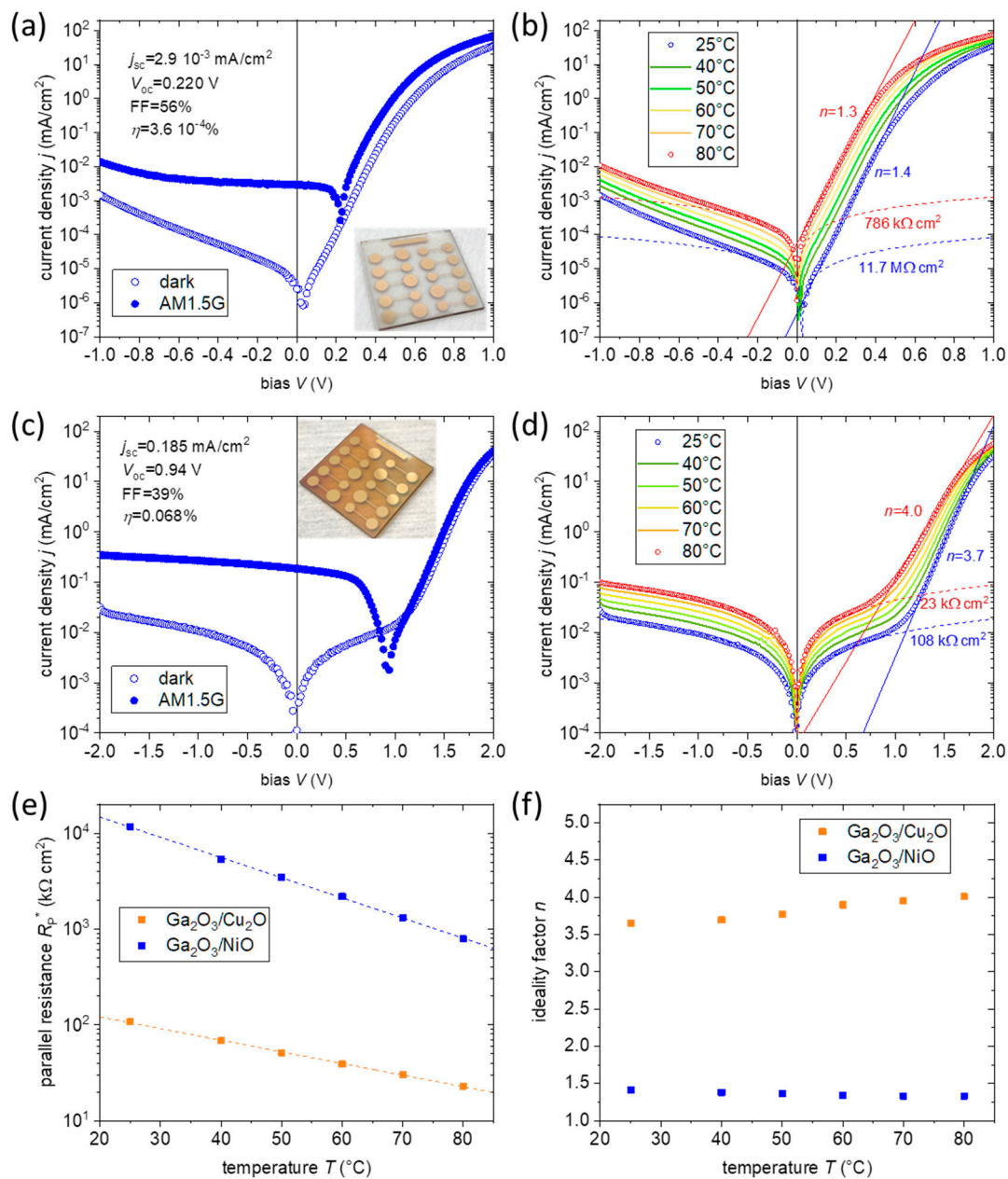


Figure 9. (a) j - V curves in dark and under illumination for the Ga₂O₃(15)/NiO(20) junction together with a photo of a sample. (b) Dark j - V curves of the Ga₂O₃(15)/NiO(20), as a function of the temperature, with the fitting for ideality factor and parallel resistance for $T = 25$ °C and 80 °C. (c) j - V curves in dark and under illumination for the Ga₂O₃(15)/Cu₂O(300) junction together with a photo of a sample. (d) Dark j - V curves of the Ga₂O₃(15)/Cu₂O(300), as a function of the temperature, with the fitting for ideality factor and parallel resistance for $T = 25$ °C and 80 °C. (e) Plot of the parallel resistance of the devices as a function of the temperature. (f) Plot of the ideality factor of the devices as a function of the temperature.

The j - V characteristics of the Cu₂O-based heterojunctions were also analyzed in a similar manner. In Figure 9c,d, typical curves for the ITO/Ga₂O₃(15)/Cu₂O(300)/Au(100) stack under dark and illuminated conditions are plotted in a semilogarithmic scale (inset shows photo of a sample). The dark j - V shows large rectification at much higher bias than

for the NiO junctions (>1000 at $|V| = 2$ V). A low parallel resistance dominates the junction properties at low and intermediate bias regimes. From the fitting of the j - V curves in the regime $(-0.5, 0.5)$ V, a parallel resistance of $108 \text{ k}\Omega \text{ cm}^2$ is extracted at ambient temperature. For all solar cells of this type, the R_P was in the range 60 – $170 \text{ k}\Omega \text{ cm}^2$.

Parallel current can be caused by the trapping and de-trapping of the carriers at defect states in the space charge region of the device. These defects can act either as recombination centers or traps depending upon the relative capture sections of the electrons and holes [46]. When charges entering the space charge region are captured in these states, they can further jump from one state to the other through tunneling or being thermally re-emitted into the conduction or valence band or to another such state. These mechanisms contribute to the R_P , while the recombination mechanism contributes to the exponential term in the current. The thermal (re)emission from the traps depends on the temperature as, with increasing temperature, the rate of trap depopulation is increased, giving rise to more free carriers. This process is described by the equation:

$$dN_t(T) = -N_t(T)\nu \exp\left(-\frac{E}{kT}\right)dt,$$

where $N_t(T)$ is the number of trapped carriers at temperature T , E the energy of the state, and ν the attempt-to-escape frequency, which is proportional to the density of states of the conduction or valence band, the capture cross-section of electrons or holes, and their thermal velocity. As elaborated in [46], this process leads to an ohmic behavior of the shunt current with respect to the bias voltage and an exponential dependence with respect to the temperature. This agrees with the observed exponential dependence of the parallel resistance on the temperature for both types of solar cells, as shown in Figure 9e.

Another important characteristic of the Cu_2O heterojunction j - V curves is the high ideality factors (>3.5) obtained in the exponential current growth regime. In this case, the ideality factor shows a moderate increase from 3.7 at ambient temperature to 4.0 at 80°C , as can be seen from Figure 9f. Such high ideality factors were reported for inorganic [47–49], organic [50], and perovskite devices [51] and have been attributed to different origins, such as (a) the existence of other rectifying junctions in the stack, (b) shunts and defects, especially at the borders of the junction areas, (c) transport across tunnel barrier, or (d) energy state disorder. Rectifying junctions can be, indeed, formed at either contact: ITO/ Ga_2O_3 or $\text{Cu}_2\text{O}/\text{Au}$. A rectifying ITO/ Ga_2O_3 junction cannot be responsible for the large ideality factor, as this would also influence the ideality factor of the heterojunctions employing NiO, which, as shown before, is not the case. A Schottky junction between Cu_2O and Au is also not probable in view of the favorable energy band alignment. However, to exclude this possibility, heterojunctions with a NiO(20) layer inserted between the Cu_2O and Au were deposited. The NiO/Au contact should be ohmic, as the $\text{Ga}_2\text{O}_3/\text{NiO}$ junctions have low ideality factors. However, the junctions with the inserted NiO have also shown ideality factors in the same range as the ones without NiO (Figure S3). From these experiments it can be concluded that contact-related rectifying junctions cannot be at the origin of the high ideality factors. Edge shunts related to the device fabrication can contribute to increasing the ideality factor; however, they would be expected to influence similarly both heterojunctions with NiO and Cu_2O , which is not the case. The ideality factor increases with decreasing Cu_2O thickness and the concomitant decrease in the device shunt resistance, as can be seen in the dark j - V curves of Figure S4 for devices with 100 and 50 nm thick Cu_2O . The main contribution to the large ideality factor is assumed to arise from the field-assisted recombination current at the $\text{Ga}_2\text{O}_3/\text{Cu}_2\text{O}$ interface due to the lowering of the potential barrier of traps or trap-assisted tunnelling at defect levels in the depletion region. With the increase in the forward bias, the electric field at the depletion region is reduced, decreasing these current contributions, which translates into an increased ideality factor [52,53].

Another important conclusion from the j - V characterization of the heterojunctions is that the ITO/ Ga_2O_3 junction should have a low energy barrier for electrons to explain the observed transport characteristics. This is in contradiction to the measured large WF

difference between ITO and Ga₂O₃ (0.6 eV), which should lead to a blocking of the electron transport and to very low currents. The question therefore arises regarding the reason for the observed unimpeded transport characteristics. An explanation is based on a significant amount of work in the literature on the type of contact between ITO and β-Ga₂O₃. Carey et al. reported ohmic contact between an *n*-type β-Ga₂O₃ wafer, with a carrier concentration of $\sim 3 \times 10^{17} \text{ cm}^{-3}$, and Ti/Au, through an intermediate 10 nm thick, sputtered ITO layer. While Ga₂O₃/Ti/Au contacts remained of Schottky type after thermal rapid annealing at 600 °C, Ga₂O₃/ITO/Ti/Au contacts showed ohmic characteristics after annealing at 500 °C, dramatically improving the electron transport across the heterointerface [54]. The creation of an ohmic contact was attributed to the interdiffusion of In, Sn, and Ga at the heterojunction. Xia et al. [55] showed the reaction of sputtered ITO with highly doped Ga₂O₃ at temperatures > 300 °C. TEM and EDX characterization showed a roughening of the heterointerface, associated with the presence of a wide reaction zone, where the In and Sn from the ITO diffuse into the Ga₂O₃, with a corresponding modification of the electrical junction characteristics. The reaction zone significantly increased after annealing at 400 °C, with the interface losing its integrity at 500 °C. These results are aligned with the present work, showing an unimpeded electron transport at the ITO/Ga₂O₃ interface, suggesting a low potential barrier for electrons. An intermixed interface is highly probable in view of the high substrate temperature used for the spray pyrolysis of Ga₂O₃ on ITO (380 °C) applied for the deposition duration of ~15 min but also the extended cooling-down phase, with ~15 min needed for the sample to reach 250 °C.

To gain more insight on the involved heterointerfaces, *C-V* measurements were realized for the NiO and Cu₂O devices, using the parallel capacitance, C_p , and parallel conductance, G_p , equivalent circuit. The measured capacitance and conductance, C_M and G_M , were corrected for the series resistance, R_S , using the approach described in [56,57]. The R_S is calculated from the capacitance and conductance values at strong accumulation ($C_{M, acc}$, $G_{M, acc}$) using the equation:

$$R_S = \frac{G_{M, acc}}{G_{M, acc}^2 + \omega^2 C_{M, acc}^2}$$

The C_p and G_p in the three-element model are calculated by the following equations:

$$C_p = \frac{(G_M^2 + \omega^2 C_M^2) \cdot C_M}{\alpha^2 + \omega^2 C_M^2}$$

$$G_p = \frac{(G_M^2 + \omega^2 C_M^2) \cdot \alpha}{\alpha^2 + \omega^2 C_M^2}$$

$$\alpha = G_M - (G_M^2 + \omega^2 C_M^2) \cdot R_S$$

Based on the above approach, the Mott–Schottky plots $\left(\frac{A}{C_p}\right)^2$ vs. V for the NiO and Cu₂O junctions and for $f = 10$ kHz are shown in Figure 10a,b, respectively. The plots show a distinct linear region that corresponds to junction depletion. From the fit and extrapolation of the linear portion of the plots, the built-in potential, V_{bi} , can be extracted, which is ~0.8 V for the NiO junction and ~1.8 V for Cu₂O. The qV_{bi} corresponds to the difference in the Fermi levels between the *n* and *p* sides of the junction. The value of 0.8 eV is not far from the WF difference between Ga₂O₃ and NiO found from the Kelvin probe measurements, while the 1.8 eV is much larger than the WF difference between Ga₂O₃ and Cu₂O from the Kelvin probe. However, as mentioned before, the formation of a CuO surface layer does not allow the estimation of the correct WF of Cu₂O by the Kelvin probe. So, the value of ~6.0 eV extracted from the Mott–Schottky plot, considering the 4.2 eV as the WF of Ga₂O₃, is assumed to be a representative WF value for the Cu₂O layer.

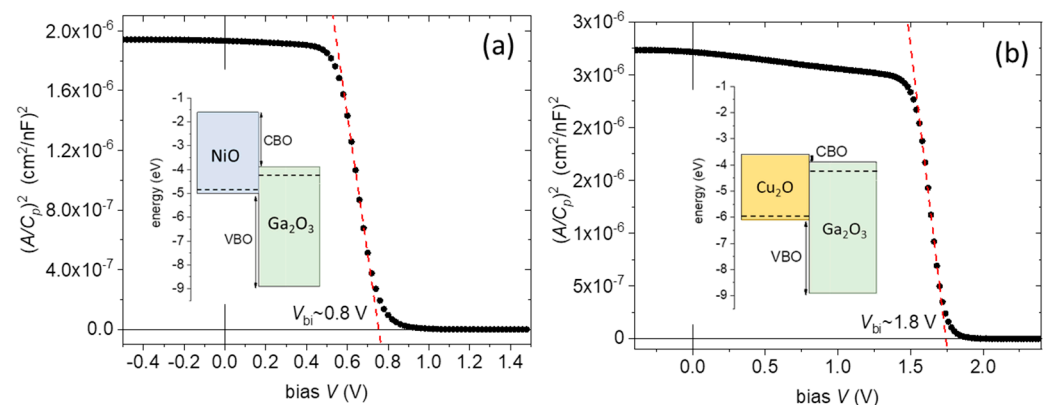


Figure 10. Mott–Schottky plots for (a) the Ga₂O₃(15)/NiO(20) junction and (b) the Ga₂O₃(15)/Cu₂O(300) junction (red lines are linear fits), together with the corresponding band diagrams, showing the anticipated CBO and VBO in both cases.

4. Conclusions

In conclusion, it was shown that high-quality *n*-Ga₂O₃, *p*-NiO and *p*-Cu₂O layers can be deposited by spray-pyrolysis (Ga₂O₃) at high temperature and RF (NiO) and reactive DC sputtering (Cu₂O) without substrate heating, with properties that make them suitable as electron- and hole-transport layers, respectively, in different types of solar cells, such as perovskite and organic, as well as optoelectronic devices. Type II heterojunctions are formed between the Ga₂O₃ and NiO or Cu₂O. Ga₂O₃/NiO junctions show large offsets for both conduction and valence bands, while, for Ga₂O₃/Cu₂O, a large offset is only present for the valence band. The rectification is high for both types of junctions. Their transport characteristics can be described by a generation-recombination channel in the first case, with an ideality factor between 1 and 2, while, in the second case, high ideality factors above 3.5 suggest significant contributions from field-assisted recombination at increased trap density in the depletion region. Further, it was shown that a low resistance ITO/Ga₂O₃ contact is formed that does not hinder electron transport, despite the expectations from the band structure of the individual layers. This is assumed to be due to the interface intermixing during the high-temperature deposition of Ga₂O₃. Low resistance contacts to Ga₂O₃ are of interest for power electronic devices, apart from the applications aforementioned. Open circuit voltage values of ~220 and ~940 mV were achieved for the NiO- and Cu₂O-based junctions, respectively. Ga₂O₃/NiO junctions absorb only in the UV region and can be applicable as photodiodes or transparent image sensors. Visible-active solar cells can be based on the Ga₂O₃/Cu₂O heterojunction. At the current state, the short circuit current is too low for practical implementation but the optimization of the absorber thickness, as well as its structural and electronic properties (e.g., grain size and charge carrier mobility) can lead to significant improvements in performance.

Supplementary Materials: The following supporting information can be downloaded at: <https://www.mdpi.com/article/10.3390/nano14030300/s1>, Figure S1: AFM images of the glass substrates; Figure S2: Initial screening of the effect of Ga₂O₃ thickness on the open circuit voltage, realized for samples with a Ga₂O₃ thickness gradient; Figure S3: *j*-*V* curve of heterojunction with inserted NiO layer between Cu₂O and Au; Figure S4: *j*-*V* curves of heterojunctions with reduced Cu₂O thickness.

Author Contributions: Conceptualization, T.D.; Formal Analysis, T.D., R.A.W., S.E., M.W. and T.F.; Investigation, T.D., R.A.W., S.E., M.W. and T.F.; Writing—Original Draft Preparation, T.D.; Writing—Review and Editing, T.D., R.A.W., S.E., M.W. and T.F.; Visualization, T.D. All authors have read and agreed to the published version of the manuscript.

Funding: This research was funded by the European Union, through the Horizon Europe project SUNREY.

Data Availability Statement: Data are contained within the article and Supplementary Material.

Conflicts of Interest: The authors declare no conflicts of interest.

References

1. Cai, X.; Hu, T.; Hou, H.; Zhu, P.; Liu, R.; Peng, J.; Luo, W.; Yu, H. A review for nickel oxide hole transport layer and its application in halide perovskite solar cells. *Mater. Today Sustain.* **2023**, *23*, 100438. [[CrossRef](#)]
2. Alkarsifi, R.; Ackermann, J.; Margeat, O. Hole transport layers in organic solar cells: A review. *J. Met. Mater. Miner.* **2022**, *32*, 1–22. [[CrossRef](#)]
3. Park, H.; Chaurasiya, R.; Jeong, B.H.; Sakthivel, P.; Park, H.J. Nickel Oxide for Perovskite Photovoltaic Cells. *Adv. Photonics Res.* **2021**, *2*, 2000178. [[CrossRef](#)]
4. Boyd, C.C.; Shallcross, R.C.; Moot, T.; Kerner, R.; Bertoluzzi, L.; Onno, A.; Kavadiya, S.; Chosy, C.; Wolf, E.J.; Werner, J.; et al. Overcoming Redox Reactions at Perovskite-Nickel Oxide Interfaces to Boost Voltages in Perovskite Solar Cells. *Joule* **2020**, *4*, 1759–1775. [[CrossRef](#)]
5. Di Girolamo, D.; Di Giacomo, F.; Matteocci, F.; Marrani, A.G.; Dini, D.; Abate, A. Progress, highlights and perspectives on NiO in perovskite photovoltaics. *Chem. Sci.* **2020**, *11*, 7746–7759. [[CrossRef](#)]
6. Chatterjee, S.; Pal, A.J. Introducing Cu₂O Thin Films as a Hole-Transport Layer in Efficient Planar Perovskite Solar Cell Structures. *J. Phys. Chem. C* **2016**, *120*, 1428–1437. [[CrossRef](#)]
7. Chuang, T.-H.; Chen, Y.-H.; Sakalley, S.; Cheng, W.-C.; Chan, C.K.; Chen, C.-P.; Chen, S.-C. Highly Stable and Enhanced Performance of p–i–n Perovskite Solar Cells via Cuprous Oxide Hole-Transport Layers. *Nanomaterials* **2023**, *13*, 1363. [[CrossRef](#)] [[PubMed](#)]
8. Dimopoulos, T. All-Oxide Solar Cells. In *The Future of Semiconductor Oxides in Next-Generation Solar Cells*; Elsevier: Amsterdam, The Netherlands, 2018; pp. 439–480, ISBN 978-0-12-811165-9.
9. Pan, L.; Liu, Y.; Yao, L.; Ren, D.; Sivula, K.; Grätzel, M.; Hagfeldt, A. Cu₂O photocathodes with band-tail states assisted hole transport for standalone solar water splitting. *Nat. Commun.* **2020**, *11*, 318. [[CrossRef](#)] [[PubMed](#)]
10. Hu, K.-H.; Wang, Z.-K.; Wang, K.-L.; Zhuo, M.-P.; Zhang, Y.; Igbari, F.; Ye, Q.-Q.; Liao, L.-S. γ -Ga₂O₃ Nanocrystals Electron-Transporting Layer for High-Performance Perovskite Solar Cells. *Sol. RRL* **2019**, *3*, 1900201. [[CrossRef](#)]
11. Lu, X.; Deng, Y.; Pei, Y.; Chen, Z.; Wang, G. Recent advances in NiO/Ga₂O₃ heterojunctions for power electronics. *J. Semicond.* **2023**, *44*, 061802. [[CrossRef](#)]
12. Kokubun, Y.; Kubo, S.; Nakagomi, S. All-oxide p–n heterojunction diodes comprising p-type NiO and n-type β -Ga₂O₃. *Appl. Phys. Express* **2016**, *9*, 091101. [[CrossRef](#)]
13. Tadjer, M.J.; Luna, L.E.; Cleveland, E.; Hobart, K.D.; Kub, F.J. (Invited) Fabrication and Characterization of β -Ga₂O₃ Heterojunction Rectifiers. *ECS Trans.* **2018**, *85*, 21–26. [[CrossRef](#)]
14. Lu, X.; Zhou, X.; Jiang, H.; Ng, K.W.; Chen, Z.; Pei, Y.; Lau, K.M.; Wang, G. 1-kV Sputtered p-NiO/n-Ga₂O₃ Heterojunction Diodes with an Ultra-Low Leakage Current Below 1 μ A/cm². *IEEE Electron Device Lett.* **2020**, *41*, 449–452. [[CrossRef](#)]
15. Gong, H.; Chen, X.; Xu, Y.; Chen, Y.; Ren, F.; Liu, B.; Gu, S.; Zhang, R.; Ye, J. Band Alignment and Interface Recombination in NiO/ β -Ga₂O₃ Type-II p-n Heterojunctions. *IEEE Trans. Electron Devices* **2020**, *67*, 3341–3347. [[CrossRef](#)]
16. Wang, Y.; Wu, C.; Guo, D.; Li, P.; Wang, S.; Liu, A.; Li, C.; Wu, F.; Tang, W. All-Oxide NiO/Ga₂O₃ p–n Junction for Self-Powered UV Photodetector. *ACS Appl. Electron. Mater.* **2020**, *2*, 2032–2038. [[CrossRef](#)]
17. Zhang, J.; Han, S.; Cui, M.; Xu, X.; Li, W.; Xu, H.; Jin, C.; Gu, M.; Chen, L.; Zhang, K.H.L. Fabrication and Interfacial Electronic Structure of Wide Bandgap NiO and Ga₂O₃ p–n Heterojunction. *ACS Appl. Electron. Mater.* **2020**, *2*, 456–463. [[CrossRef](#)]
18. Minami, T.; Nishi, Y.; Miyata, T. High-Efficiency Cu₂O-Based Heterojunction Solar Cells Fabricated Using a Ga₂O₃ Thin Film as N-Type Layer. *Appl. Phys. Express* **2013**, *6*, 044101. [[CrossRef](#)]
19. Lee, Y.S.; Chua, D.; Brandt, R.E.; Siah, S.C.; Li, J.V.; Mailoa, J.P.; Lee, S.W.; Gordon, R.G.; Buonassisi, T. Atomic Layer Deposited Gallium Oxide Buffer Layer Enables 1.2 V Open-Circuit Voltage in Cuprous Oxide Solar Cells. *Adv. Mater.* **2014**, *26*, 4704–4710. [[CrossRef](#)] [[PubMed](#)]
20. Chua, D.; Kim, S.B.; Gordon, R. Enhancement of the open circuit voltage of Cu₂O/Ga₂O₃ heterojunction solar cells through the mitigation of interfacial recombination. *AIP Adv.* **2019**, *9*, 055203. [[CrossRef](#)]
21. Benz, S.L.; Becker, M.; Polity, A.; Chatterjee, S.; Klar, P.J. Determining the band alignment of copper-oxide gallium-oxide heterostructures. *J. Appl. Phys.* **2021**, *129*, 115305. [[CrossRef](#)]
22. Winkler, N.; Wibowo, R.A.; Kautek, W.; Ligorio, G.; List-Kratochvil, E.J.W.; Dimopoulos, T. Nanocrystalline Ga₂O₃ films deposited by spray pyrolysis from water-based solutions on glass and TCO substrates. *J. Mater. Chem. C* **2019**, *7*, 69–77. [[CrossRef](#)]
23. Ebner, D.; Bauch, M.; Dimopoulos, T. High performance and low cost transparent electrodes based on ultrathin Cu layer. *Opt. Express* **2017**, *25*, A240. [[CrossRef](#)]
24. Salunkhe, P.; AV, M.A.; Kekuda, D. Structural, spectroscopic and electrical properties of dc magnetron sputtered NiO thin films and an insight into different defect states. *Appl. Phys. A* **2021**, *127*, 390. [[CrossRef](#)]
25. Potlog, T.; Ghimpu, L.; Suman, V.; Pantazi, A.; Enachescu, M. Influence of RF sputtering power and thickness on structural and optical properties of NiO thin films. *Mater. Res. Express* **2019**, *6*, 096440. [[CrossRef](#)]
26. Lee, H.; Huang, Y.-T.; Horn, M.W.; Feng, S.-P. Engineered optical and electrical performance of rf-sputtered undoped nickel oxide thin films for inverted perovskite solar cells. *Sci. Rep.* **2018**, *8*, 5590. [[CrossRef](#)]

27. Dolai, S.; Das, S.; Hussain, S.; Bhar, R.; Pal, A.K. Cuprous oxide (Cu₂O) thin films prepared by reactive d.c. sputtering technique. *Vacuum* **2017**, *141*, 296–306. [[CrossRef](#)]
28. Azanza Ricardo, C.L.; D’Incau, M.; Leoni, M.; Malerba, C.; Mittiga, A.; Scardi, P. Structural properties of RF-magnetron sputtered Cu₂O thin films. *Thin Solid Film.* **2011**, *520*, 280–286. [[CrossRef](#)]
29. Bordun, O.M.; Kukharskyy, I.Y.; Bordun, B.O.; Lushchanets, V.B. Dispersion of Refractive Index of β-Ga₂O₃ Thin Films. *J. Appl. Spectrosc.* **2014**, *81*, 771–775. [[CrossRef](#)]
30. Mahmoodinezhad, A.; Janowitz, C.; Naumann, F.; Plate, P.; Gargouri, H.; Henkel, K.; Schmeißer, D.; Flege, J.I. Low-temperature growth of gallium oxide thin films by plasma-enhanced atomic layer deposition. *J. Vac. Sci. Technol. A* **2020**, *38*, 022404. [[CrossRef](#)]
31. Park, J.-W.; Choi, K.N.; Baek, S.H.; Chung, K.S.; Lee, H. Optical Properties of NiO Thin Films Grown by Using Sputtering Deposition and Studied with Spectroscopic Ellipsometry. *J. Korean Phy. Soc.* **2008**, *52*, 1868–1876. [[CrossRef](#)]
32. Ito, T.; Kawashima, T.; Yamaguchi, H.; Masumi, T.; Adachi, S. Optical Properties of Cu₂O Studied by Spectroscopic Ellipsometry. *J. Phys. Soc. Jpn.* **1998**, *67*, 2125–2131. [[CrossRef](#)]
33. Tauc, J. Optical properties and electronic structure of amorphous Ge and Si. *Mater. Res. Bull.* **1968**, *3*, 37–46. [[CrossRef](#)]
34. Ruske, F.; Wimmer, M.; Köppel, G.; Pflug, A.; Rech, B. *Optical Characterization of High Mobility Polycrystalline ZnO:Al Films*; Rogers, D.J., Ed.; SPIE OPTO: San Francisco, CA, USA, 2012; p. 826303.
35. Wang, Y.; Bruyère, S.; Kumagai, Y.; Tsunoda, N.; Oba, F.; Ghanbaja, J.; Sun, H.; Dai, B.; Pierson, J.-F. Tuning the optical band gap and electrical properties of NiO thin films by nitrogen doping: A joint experimental and theoretical study. *RSC Adv.* **2022**, *12*, 21940–21945. [[CrossRef](#)]
36. Predanocny, M.; Hotový, I.; Čaplovičová, M. Structural, optical and electrical properties of sputtered NiO thin films for gas detection. *Appl. Surf. Sci.* **2017**, *395*, 208–213. [[CrossRef](#)]
37. Terlemezoglu, M.; Surucu, O.; Isik, M.; Gasanly, N.M.; Parlak, M. Temperature-dependent optical characteristics of sputtered NiO thin films. *Appl. Phys. A* **2022**, *128*, 50. [[CrossRef](#)]
38. Malerba, C.; Biccari, F.; Leonor Azanza Ricardo, C.; D’Incau, M.; Scardi, P.; Mittiga, A. Absorption coefficient of bulk and thin film Cu₂O. *Sol. Energy Mater. Sol. Cells* **2011**, *95*, 2848–2854. [[CrossRef](#)]
39. Lee, S.H. The Characteristics of Cu₂O Thin Films Deposited Using RF-Magnetron Sputtering Method with Nitrogen-Ambient. *ETRI J.* **2013**, *35*, 1156–1159. [[CrossRef](#)]
40. Wang, Y.; Miska, P.; Pilloud, D.; Horwat, D.; Mücklich, F.; Pierson, J.F. Transmittance enhancement and optical band gap widening of Cu₂O thin films after air annealing. *J. Appl. Phys.* **2014**, *115*, 073505. [[CrossRef](#)]
41. Islam, M.A.; Wahab, Y.A.; Khandaker, M.U.; Alsubaie, A.; Almalki, A.S.A.; Bradley, D.A.; Amin, N. High Mobility Reactive Sputtered CuxO Thin Film for Highly Efficient and Stable Perovskite Solar Cells. *Crystals* **2021**, *11*, 389. [[CrossRef](#)]
42. Deuermeier, J.; Liu, H.; Rapenne, L.; Calmeiro, T.; Renou, G.; Martins, R.; Muñoz-Rojas, D.; Fortunato, E. Visualization of nanocrystalline CuO in the grain boundaries of Cu₂O thin films and effect on band bending and film resistivity. *APL Mater.* **2018**, *6*, 096103. [[CrossRef](#)]
43. Young, K.F.; Frederikse, H.P.R. Compilation of the Static Dielectric Constant of Inorganic Solids. *J. Phys. Chem. Ref. Data* **1973**, *2*, 313–410. [[CrossRef](#)]
44. Zhang, L.; McMillon, L.; McNatt, J. Gas-dependent bandgap and electrical conductivity of Cu₂O thin films. *Sol. Energy Mater. Sol. Cells* **2013**, *108*, 230–234. [[CrossRef](#)]
45. Sah, C.; Noyce, R.; Shockley, W. Carrier Generation and Recombination in P-N Junctions and P-N Junction Characteristics. *Proc. IRE* **1957**, *45*, 1228–1243. [[CrossRef](#)]
46. Banerjee, S.; Anderson, W.A. Temperature dependence of shunt resistance in photovoltaic devices. *Appl. Phys. Lett.* **1986**, *49*, 38–40. [[CrossRef](#)]
47. Shah, J.M.; Li, Y.-L.; Gessmann, T.; Schubert, E.F. Experimental analysis and theoretical model for anomalously high ideality factors ($n \gg 2.0$) in AlGaIn/GaN p-n junction diodes. *J. Appl. Phys.* **2003**, *94*, 2627–2630. [[CrossRef](#)]
48. Breitenstein, O.; Bauer, J.; Lotnyk, A.; Wagner, J.-M. Defect induced non-ideal dark—Characteristics of solar cells. *Superlattices Microstruct.* **2009**, *45*, 182–189. [[CrossRef](#)]
49. Jeong, S.; Song, S.H.; Nagaich, K.; Campbell, S.A.; Aydil, E.S. An analysis of temperature dependent current–voltage characteristics of Cu₂O–ZnO heterojunction solar cells. *Thin Solid Film.* **2011**, *519*, 6613–6619. [[CrossRef](#)]
50. Xiong, C.; Sun, J.; Yang, H.; Jiang, H. Real reason for high ideality factor in organic solar cells: Energy disorder. *Sol. Energy* **2019**, *178*, 193–200. [[CrossRef](#)]
51. Mahapatra, A.; Parikh, N.; Kumar, P.; Kumar, M.; Prochowicz, D.; Kalam, A.; Tavakoli, M.M.; Yadav, P. Changes in the Electrical Characteristics of Perovskite Solar Cells with Aging Time. *Molecules* **2020**, *25*, 2299. [[CrossRef](#)] [[PubMed](#)]
52. Kaminski, A.; Marchand, J.J.; El Omari, H.; Laugier, A.; Le, Q.N.; Sarti, D. Conduction processes in silicon solar cells. In Proceedings of the Conference Record of the Twenty Fifth IEEE Photovoltaic Specialists Conference, Washington, DC, USA, 13–17 May 1996; IEEE: Washington, DC, USA, 1996; pp. 573–576.
53. Breitenstein, O.; Bauer, J.; Altermatt, P.P.; Ramspeck, K. Influence of Defects on Solar Cell Characteristics. *Solid State Phenom.* **2009**, *156–158*, 1–10. [[CrossRef](#)]
54. Carey, P.H.; Yang, J.; Ren, F.; Hays, D.C.; Pearton, S.J.; Kuramata, A.; Kravchenko, I.I. Improvement of Ohmic contacts on Ga₂O₃ through use of ITO-interlayers. *J. Vac. Sci. Technol. B* **2017**, *35*, 061201. [[CrossRef](#)]

55. Xia, X.; Xian, M.; Ren, F.; Rasel, M.A.J.; Haque, A.; Pearton, S.J. Thermal Stability of Transparent ITO/n-Ga₂O₃/n+-Ga₂O₃/ITO Rectifiers. *ECS J. Solid State Sci. Technol.* **2021**, *10*, 115005. [[CrossRef](#)]
56. Tuğluoğlu, N.; Karadeniz, S.; Birkan Selçuk, A.; Bilge Ocak, S. Effect of oxide thickness on the capacitance and conductance characteristics of MOS structures. *Phys. B Condens. Matter* **2007**, *400*, 168–174. [[CrossRef](#)]
57. Zhang, X.; Zhu, H.; Cheng, C.; Yu, T.; Zhang, D.; Zhong, H.; Li, X.; Cheng, Y.; Xu, X.; Cheng, L.; et al. Single frequency correction based on three-element model for thin dielectric MOS capacitor. *Solid-State Electron.* **2017**, *129*, 97–102. [[CrossRef](#)]

Disclaimer/Publisher's Note: The statements, opinions and data contained in all publications are solely those of the individual author(s) and contributor(s) and not of MDPI and/or the editor(s). MDPI and/or the editor(s) disclaim responsibility for any injury to people or property resulting from any ideas, methods, instructions or products referred to in the content.